International Journal of Solids and Structures 49 (2012) 3496–3506

Contents lists available at SciVerse ScienceDirect

International Journal of Solids and Structures

journal homepage: www.elsevier.com/locate/ijsolstr

Determination of anisotropy and material hardening for aluminum sheet metal

Nicolas Tardif [1], Stelios Kyriakides *

Research Center for Mechanics of Solids, Structures & Materials, WRW 110, C0600, The University of Texas at Austin, Austin, TX 78712, USA

ARTICLE INFO

Article history:
Available online 3 February 2012

Keywords:
Sheet metal
Anisotropy
Hardening law
Tensile test
Necking
Localization

ABSTRACT

Sheet metal forming, crushing simulations of thin-walled structures, and other large deformation processes require knowledge of the material stress–strain behavior to large strains. The material response of sheets measured in the traditional uniaxial tension test usually terminates at strains of a few percent due to necking. It can be extrapolated to some degree using results from biaxial tests (e.g., equibiaxial tension) but not to sufficiently large strains. This work shows a systematic methodology that uses a combination of experiment and analysis to extract the material response at much larger strains. This is achieved by accurately following the deformation in the necked region of a custom tensile test specimen. The test is simulated numerically using a 3D FE model and the material response is iteratively extrapolated until the calculated and measured force-elongation match. For the Al-6061-T6 sheet metal of interest, the process is complicated by inherent anisotropies introduced during the rolling of the sheets. The anisotropy is characterized by a set of uniaxial and biaxial tests conducted in parallel. The results are used to calibrate the 18-parameter non-quadratic Yld2004-3D yield function. The calibrated yield function is then used to simulate the tensile test. The material hardening is iteratively adjusted by comparing the measured and calculated force–displacement response and validated by the corresponding measured strains and shape of the neck.

1. Introduction

Sheet metal forming, crushing simulations of thin-walled structures, and other large deformation processes require knowledge of the material stress–strain behavior to large strains. The material response of sheets measured in traditional uniaxial tension tests usually terminates at strains of a few percent due to necking. The stress–strain response can be extrapolated to some degree using results from biaxial tests (e.g., bulge test) but the extrapolation remains inadequate for many applications especially ones where the model is required to follow the evolution of localization and the prediction of failure. The most common response to this need is to extrapolate the measured response using one of the commonly adopted fits (e.g., power-law, Voce (1948), Swift (1952)). This of course is a highly inadequate solution especially for problems involving local or global instabilities, which are highly dependent on the instantaneous tangent modulus. A more well-grounded approach is to use combination of experiment and analysis to "extract" the material response from inside the neck that develops in tensile tests on ductile metals. This approach started with the pioneering work of Bridgman (1944) who proposed an approximate analytical method for extrapolating the stress–strain response based on measurement of the diameter as well as the profile radius of the neck of a round specimen. Chen (1971) pushed the subject forward by formulating the finite deformation elasto-plastic necking problem, which he solved approximately. Norris et al. (1978) used an axisymmetric FE solution to analyze the deformation and stress-state in the neck more thoroughly and iteratively modified the true stress–strain response adopted until the force–displacement response recorded experimentally was matched. Their results showed significant difference in the triaxial state of stress in the neck from that of Bridgman's model and some difference in the extrapolated true stress–strain response.

The corresponding extrapolation from tensile tests on thin rectangular specimens extracted from sheet metal is more complicated because beyond the load maximum the specimen first develops a diffuse neck but subsequently inclined bands of localized deformation show up inside the neck making the deformation truly three-dimensional. Efforts to analyze the problem numerically and/or approximate methods for extracting the material response are too many to list here. Instead, we list the works that we found most useful in our attempt at the problem that include Tvergaard (1993), Zhang et al. (1999), Scheider et al. (2004), Cai et al. (2007) among others.

This study is focused on the large deformation and failure of aluminum alloys in general and Al-6061-T6 in particular. During the past two decades it has been shown that the yielding of Al alloys is best represented by non-quadratic yield functions (e.g.,

* Corresponding author.
E-mail address: skk@mail.utexas.edu (S. Kyriakides).
[1] Presently at Civil and Environmental Engineering Laboratory, INSA Lyon, France.

0020-7683/$ - see front matter © 2012 Elsevier Ltd. All rights reserved.
doi:10.1016/j.ijsolstr.2012.01.011

Hosford (1972), Hill (1979, 1990)). The implementation of such yield functions is further complicated by inherent plastic anisotropies. Anisotropy can be accounted for by using one of the more advanced yield functions most of which build on Hosford's yield function (1972, 1979) (e.g., Barlat and Lian, 1989; Karafillis and Boyce, 1993; Barlat et al., 2003; Banabic et al., 2005; Barlat et al., 2005).

In our recent work on burst failure of Al-alloy tubes under biaxial stress paths, we found that correct calibration and implementation of such advanced non-quadratic anisotropic yield functions is essential for accurate prediction of the corresponding strain paths as well as of the localization that precedes burst (Korkolis and Kyriakides, 2008a,b, 2009) for Al-6260-T4; Korkolis et al. (2010) for Al-6061-T6). Furthermore, the same calibrated models were shown to be necessary tools for prediction of slow-growing local depressions that evolve into local necks that lead to failure in hydroforming (Korkolis and Kyriakides, 2011) and crushing of Al-alloy tubes (Giagmouris et al., 2010). Another requirement for high quality predictions, especially of localized deformations, was an accurate extrapolation of the material stress–strain response to large strains.

With this background in the present study we use experiment and analysis to extrapolate the measured tensile stress–strain response of Al-6061-T6 sheet and simultaneously consider the effect of anisotropy on the extrapolation (see Dunand and Mohr (2010) for a similar effort for TRIP780 steel). This is achieved by conducting in parallel a set of tests that are required to calibrate the 3-D anisotropic yield function of Barlat et al. (2005) hitherto referred to as *Yld04-3D*.

2. Experimental

2.1. Tensile test

The stress–strain response of the material was measured in a tensile test on the specially designed specimen shown in Fig. 1. It was cut from a nominally 0.100 in (2.5 mm) plate along the rolling direction using wire EDM (actual thickness of specimen 0.0955 in—2.426 mm). It has an overall length of 6.5 in (165 mm) and a 3.5 in (89 mm) long test section. In order to ensure that necking and localization occur at mid-span, a large radius (204.17 in—5186 mm) was machined into the sides of the specimen as shown schematically in the figure. Thus, at the ends the test section was 0.450 in (11.43 mm) wide while at mid-span 0.434 in (11.02 mm—w_0).

The tension test was conducted under displacement control in an electromechanical testing machine run at a rate of 0.02 in/min (0.5 mm/min), which during the uniform part of the deformation resulted in a strain rate of $1.1 \times 10^{-4}s^{-1}$. The specimen was secured to the testing machine with carefully aligned hydraulic grips. In addition to monitoring the overall applied displacement, the deformation in the middle of the test section was monitored with a 2.0 in (50.8 mm) extensometer. To help us evaluate the accuracy of the inverse method used to extrapolate the stress–strain response, Digital Image Correlation (DIC) was used to monitor the in-plane deformation in the test section. To enable the DIC a fine speckle pattern was painted onto one side of the specimen (undercoat of white paint with black spray over it). The deformation of the speckle pattern was monitored with a digital camera equipped with a timer that recorded a frame every 2 s (4288 × 2848 pixel resolution). The recorded images were also used to monitor the shape of the diffuse neck that develops after the load maximum. For optimum detection, the edges of the specimen were painted mat white, the specimen was lit uniformly, and a dark background was used. The reproduction of the shape of the neck will form a second evaluation criterion of the numerical procedure used to extract the stress–strain response.

Fig. 2 shows the measured engineering stress-elongation response in one of the tensile tests performed. Here, the recorded force is divided by the initial minimum cross sectional area of the specimen; δ is the change in length of the monitored gage length and $2L_g$ is its initial length (2.0 in—50.8 mm). The response exhibits a linearly elastic region followed by a relatively tight yielding knee and by a strain regime characterized by mild hardening; a load maximum develops at a strain of nearly 7.0% (indicated on the response by "^", point ①) (material has an elastic modulus of 10.2 Msi—70.5 GPa—and a 0.2% strain offset yield stress of 46.58 ksi–321.2 MPa). Beyond the maximum the deformation localizes first into a diffuse neck around the mid-span and later into inclined localized bands inside the neck. This region will be the subject of further analysis using the results of DIC and edge detection. Marked on the response are six points at which the deformation will be analyzed.

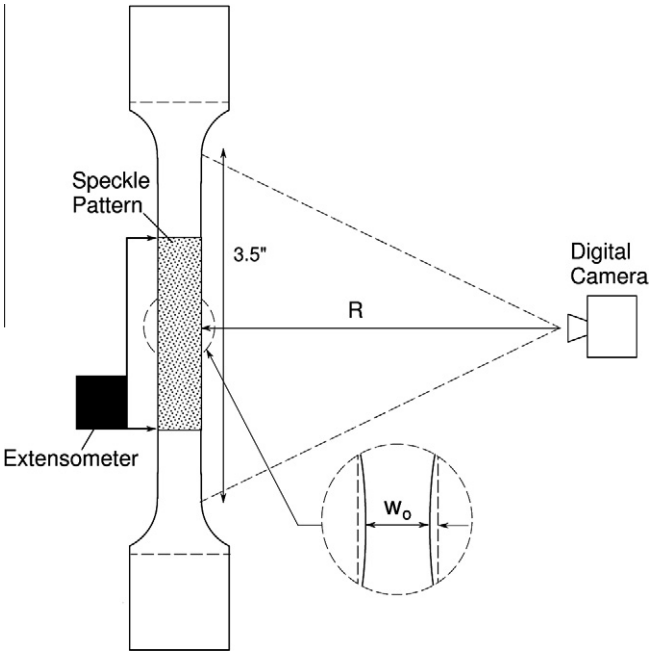

Fig. 1. Custom flat tensile test specimen with large radius built into the sides.

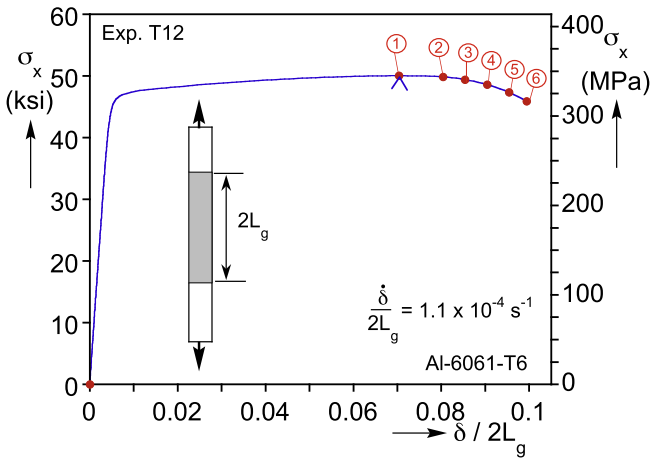

Fig. 2. Measured engineering stress-elongation response for Al-6061-T6 sheet in the rolling direction. Deformation in the necking region will be analyzed at marked points on the descending part.

We start with the edge detection results. Fig. 3 shows a photograph of the necked region of specimen T12 at the termination of the test (point ⑥ in Fig. 2 at $\delta/2L_g = 0.100$). The fine speckle pattern as well as the specially prepared edges can be clearly seen. The edges of the specimen were identified from the digital images using the Scilab4.1 software and the image processing toolbox SIP. The edge could be resolved to the nearest few pixels of the image using a Sobel filter and thus two bounds will be identified for each. The loci of the two bounds of the positions of each edge were then smoothened by first locally fitting each locus with order 3 polynomials and then minimizing the least squares error between the data and the local polynomial. The x–y profiles of the left and right edges are plotted in the Fig. 3 (w_o is the width at the center of the test section). The deepest part of the neck is seen to extend over a length that is of the order of 1.5 times the width.

Fig. 4 shows sets of the x-y profiles of the two edges corresponding to the six points marked on the $\sigma_x - \delta$ response in Fig. 2. They are identified by the values of the corresponding displacement $\delta/2L_g$. Included are also the initial shapes of the edges (i.e., at $\delta = 0$), which clearly show the large radius machined into the specimen. The next profiles corresponding to the load maximum (①) have moved inwards due to the Poisson effect but show no localization. Profiles corresponding to points ② to ⑥, on the descending part of the response in Fig. 2, show an increasingly deepening neck with a sharpening curvature at the narrowest point. It is interesting to also observe that, as expected, as the neck grows the edges away from the necking zone do not move significantly.

Next we turn to the in-plane strains, which are extracted from the digital images using the *Aramis* software. Fig. 5 shows in color contours the axial logarithmic strain (e_x) in the central part of the specimen corresponding to points ① to ⑥ on the response (note different color codes of images). Fig. 6a shows plots of the axial strain along the centerline of the specimen over a length of nearly $4w_0$ for the six points. Fig. 6b shows the corresponding ratios of the transverse strain to the axial strain along the same line. Image ① in Fig. 5 exhibits a gradient along the length due to the small variation in cross sectional area but no variation across the width or localization. The corresponding centerline trajectory of e_x in Fig. 6a also shows no localization. Images ② and ③ show increasing concentration of strain in the central section as well as variation of strain across the width. The corresponding centerline strain plots in Fig. 6a clearly show the strain becoming increasingly more localized. In images ④ to ⑥ the local strain increases and x-shaped deformation is superimposed on that of the neck. The extent of the local strains is quantified in the centerline e_x trajectories. The strain ratio e_y/e_x hovers just below 0.4 for most of the length, a first sign of plastic anisotropy (for the larger values of δ the strain ratio has a small dip near the center of the specimen, which here is partially masked by the noise in the data).

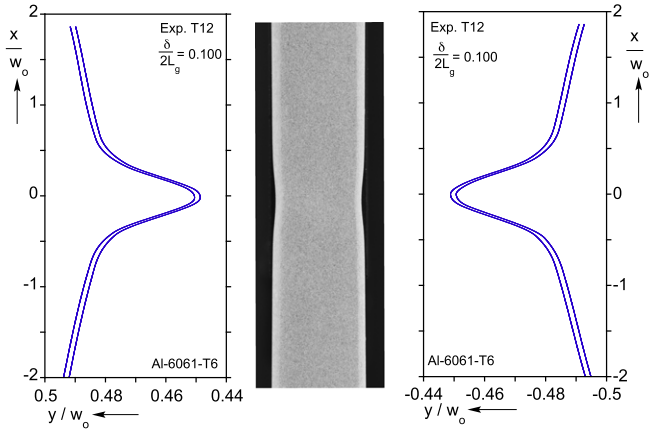

Fig. 3. Boundaries of left and right specimen edges at point ⑥ on the response and a photograph of the actual specimen.

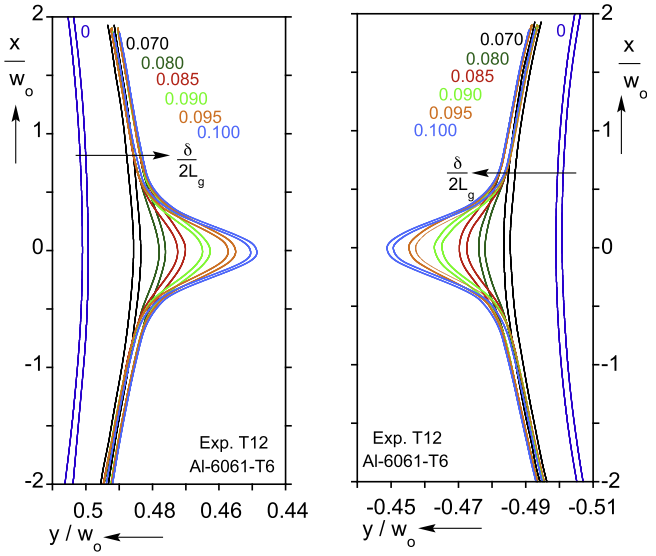

Fig. 4. Boundaries of left and right specimen edges corresponding to six points marked on the response in Fig. 2 illustrating the evolution of diffuse necking.

2.2. Characterization of anisotropy

The deformation in the neck is fully three-dimensional and therefore in the inverse method that we will follow the tensile specimen will be modeled with solid finite elements. Furthermore, we intend to use a non-quadratic yield function and the anisotropy will be introduced via the 18-parameter Yld04-3D function of Barlat et al. (2005) that is outlined in Section 3. The parameters were determined using the series of tests on specimens extracted from sheet metal as recommended in Barlat et al. (2005) with one exception. They include measurement of the flow stresses and r-values in seven tension tests on specimens extracted at 15° intervals between the rolling and transverse direction (see Fig. 7a; x- and 0° correspond to rolling direction), and the r-values at different levels of compression from a disk compression test (Fig. 7b). We did not have access to a bulge testing facility so biaxial stress data were obtained from three plane strain tests on specimens extracted as shown in Fig. 7c (45° test recommended in Aretz et al. (2010)). This is done realizing that such tests are not true substitutes to an equibiaxial test, as well as that small errors can result in the data extracted.

The tensile and disc compression tests are quite standard so we limit attention to just presentation of the results. Fig. 8a shows truncated the true stress-logarithmic strain responses from the seven tensile tests and Fig. 8b the axial vs. transverse strain plots. The in-plane anisotropy for this material is mild and thus the difference between the seven responses is modest. In the disc compression tests the principal diameters of the compressed discs were measured at different levels of normal strain. Fig. 9 shows a plot of the average logarithmic strains in the principal directions of anisotropy (x', y'). The data shows a linear relationship that differs from the 1:1 direction.

The plane strain tests involve some innovativeness and consequently deserve more detailed attention. The specimen geometry shown in Fig. 10a was determined from FE calculations aimed at ensuring near zero transverse strain at the center of the test section. The design is influenced by similar efforts by others reported in the literature, but the side grooves are somewhat deeper than is customary and have a larger radius (Wagoner, 1981). A speckle pattern was painted at mid-span to enable full-field DIC monitoring of the

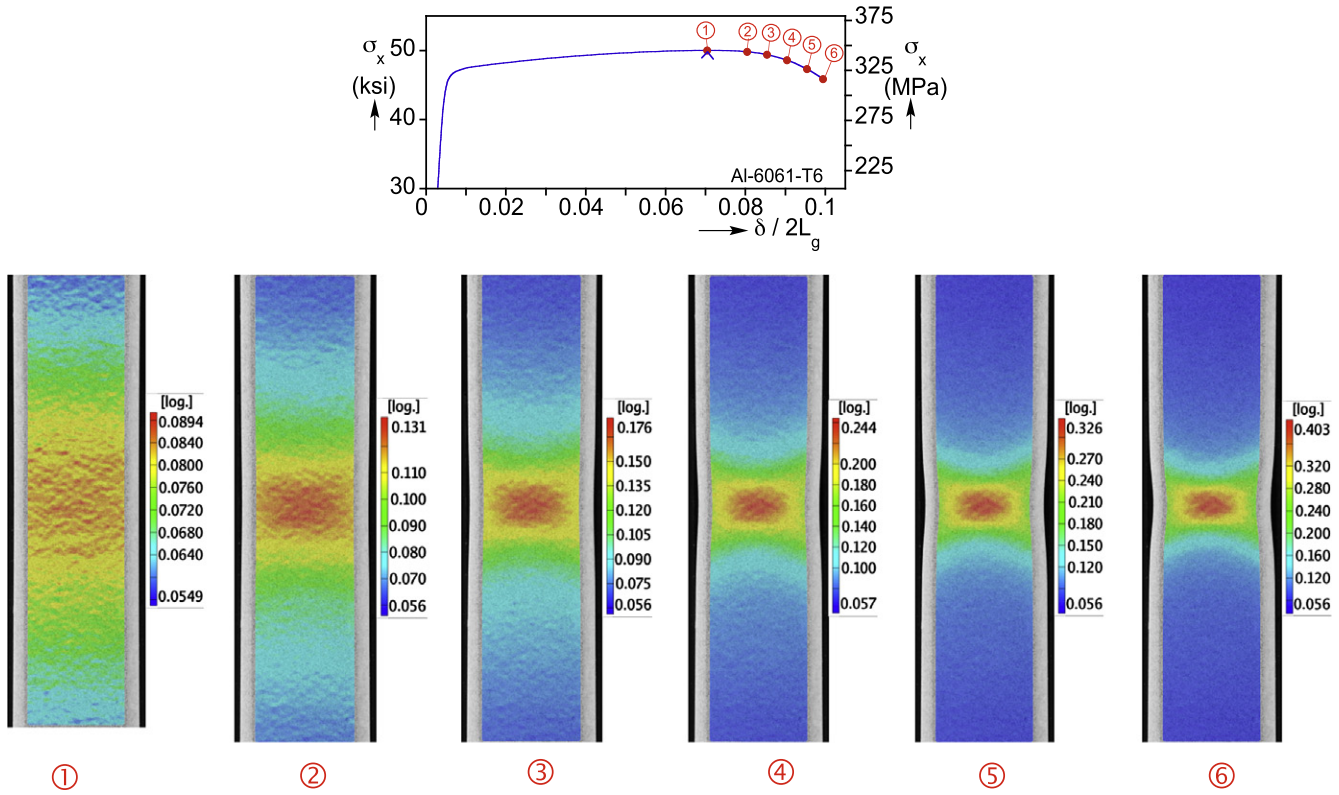

Fig. 5. Contours of axial strain from DIC corresponding to six points marked on the response. Note the different scales and the cross-shaped localization that develops.

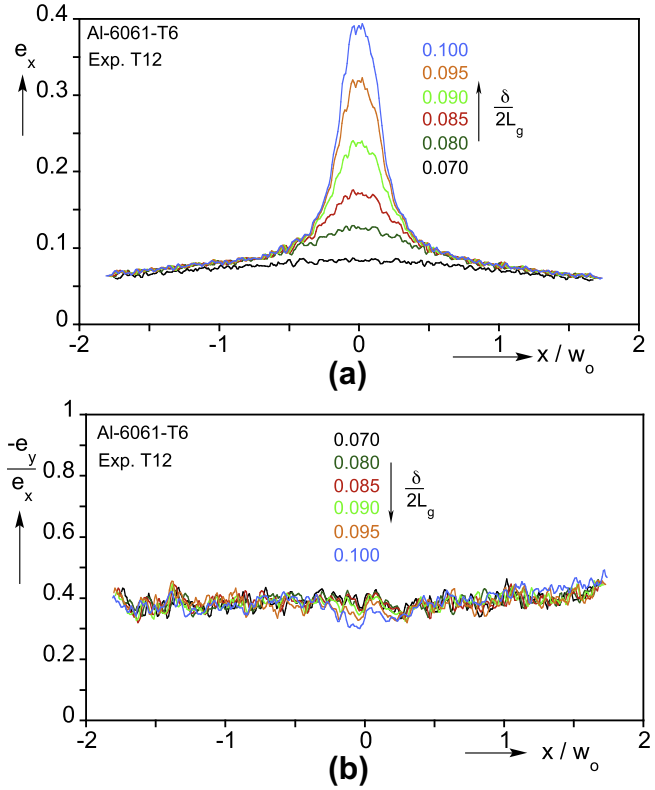

Fig. 6. (a) Measured axial strains and (b) transverse strain ratios along the centerline of the test specimen.

in-plane strains. In addition, a small strain gage (length 0.062 in–1.59 mm) was installed on the backside to monitor the axial strain at the center and act as an independent check of the DIC measurements.

The tests were performed in an electromechanical testing machine equipped with hydraulic grips. The machine was run under displacement control at a rate that produced a strain rate of approximately 10^{-4} s^{-1} during the early parts of the tests (note that this material is essentially insensitive to rate at low strain rates). The results showed nearly zero transverse strain in the center of the specimen while the strain gage and DIC axial strains were in very good agreement (strain gage usually fails after plastic deformation of a few percent). The axial true (Cauchy) stress (τ_x) is evaluated from the recorded force by dividing by the current cross sectional area at mid-span $A = A_o/(1+\bar{\varepsilon}_x)$, where $\bar{\varepsilon}_x$ is the average value of axial strain recorded by DIC across the width at the center of the test section ($x = 0$) and A_o is the initial cross sectional area ($w_0 \times t$). Fig. 10b shows the true stress-logarithmic strain responses recorded in the three directions (e_x, measured at the center of the test section). Anisotropy is responsible for the small differences between them.

3. Anisotropic constitutive model

3.1. The Yld04 model (Barlat et al., 2005)

The model is based on the non-quadratic isotropic yield function of Hosford (1972), which in terms of the principal values of the stress deviator is written as:

$$|s_1 - s_2|^k + |s_2 - s_3|^k + |s_3 - s_1|^k = 2\sigma_o^k \tag{1}$$

Anisotropy is introduced by two linear transformations, which are used to construct the tensors $\boldsymbol{S}', \boldsymbol{S}''$ from the actual stress tensor $\boldsymbol{\sigma}$ as follows:

$$\boldsymbol{S}' = \boldsymbol{C}'\boldsymbol{s} = \boldsymbol{C}'\boldsymbol{T}\boldsymbol{\sigma} = \boldsymbol{L}'\boldsymbol{\sigma} \quad \text{and} \quad \boldsymbol{S}'' = \boldsymbol{C}''\boldsymbol{s} = \boldsymbol{C}''\boldsymbol{T}\boldsymbol{\sigma} = \boldsymbol{L}''\boldsymbol{\sigma} \tag{2}$$

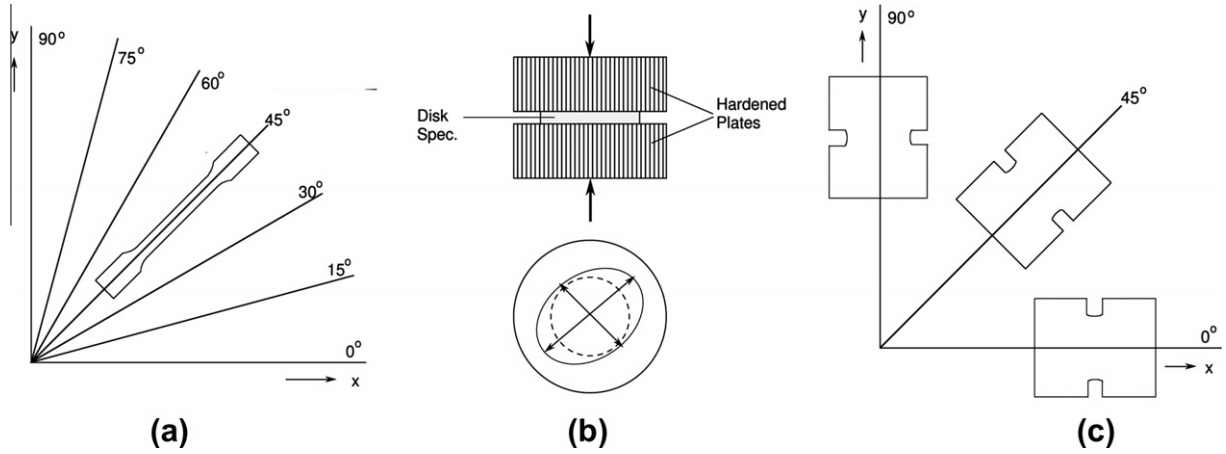

Fig. 7. Test specimens used to calibrate the Yld04-3D anisotropic constitutive model. (a) Seven tensile specimens, (b) disk compression test, and (c) three plane strain specimens.

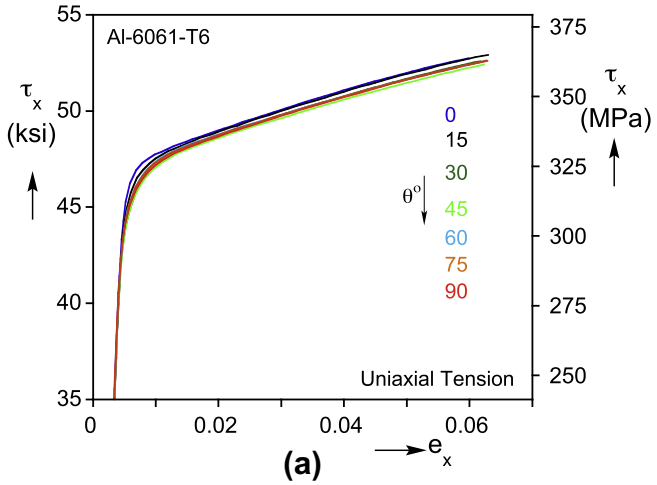

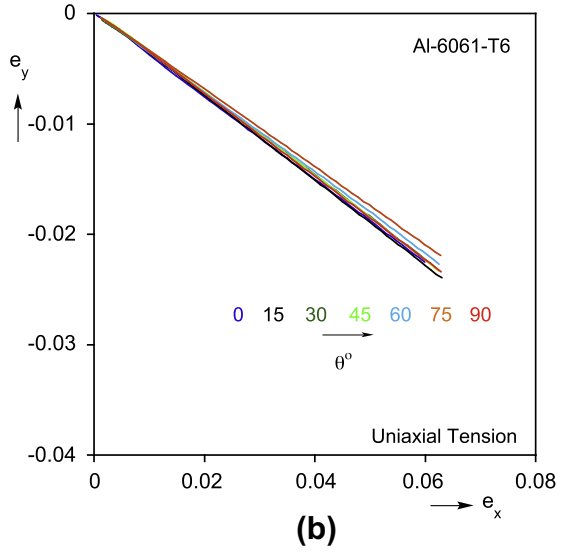

Fig. 8. Results from tensile tests in seven directions ($0^\circ \equiv$ rolling direction): (a) True stress-logarithmic strain responses and (b) transverse vs. axial strain.

where $\boldsymbol{C}'$, $\boldsymbol{C}''$, $\boldsymbol{T}$, $\boldsymbol{L}'$ and $\boldsymbol{L}''$ are transformation matrices through which anisotropy is introduced. $\boldsymbol{T}$ is the standard linear transformation of

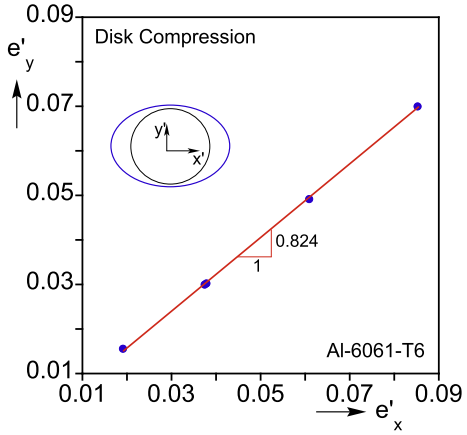

Fig. 9. Principal strains measured at different levels of disk compressions.

$\boldsymbol{\sigma}$ to its deviator $\boldsymbol{s}$, while the $\boldsymbol{C}'$ and $\boldsymbol{C}''$ contain 18 anisotropy parameters as follows:

$$\boldsymbol{C}' = \begin{bmatrix} 0 & -c'_{12} & -c'_{13} & 0 & 0 & 0 \\ -c'_{21} & 0 & -c'_{23} & 0 & 0 & 0 \\ -c'_{31} & -c'_{32} & 0 & 0 & 0 & 0 \\ 0 & 0 & 0 & c'_{44} & 0 & 0 \\ 0 & 0 & 0 & 0 & c'_{55} & 0 \\ 0 & 0 & 0 & 0 & 0 & c'_{66} \end{bmatrix} \tag{3a}$$

and

$$\boldsymbol{C}'' = \begin{bmatrix} 0 & -c''_{12} & -c''_{13} & 0 & 0 & 0 \\ -c''_{21} & 0 & -c''_{23} & 0 & 0 & 0 \\ -c''_{31} & -c''_{32} & 0 & 0 & 0 & 0 \\ 0 & 0 & 0 & c''_{44} & 0 & 0 \\ 0 & 0 & 0 & 0 & c''_{55} & 0 \\ 0 & 0 & 0 & 0 & 0 & c''_{66} \end{bmatrix} \tag{3b}$$

The principal values of the linearly transformed stress tensors $\boldsymbol{S}'$ and $\boldsymbol{S}''$, respectively (S'_1, S'_2, S'_3) and $(S''_1, S''_2, 2S''_3)$, are evaluated analytically using Cardan's method. The solutions as well as the first and second derivatives of the yield function with respect to the stress components, which are required for the flow rule and the consistent tangent modulus, are given in Barlat et al. (2005) and Yoon et al. (2006). The Yld2004-3D yield function is then written as:

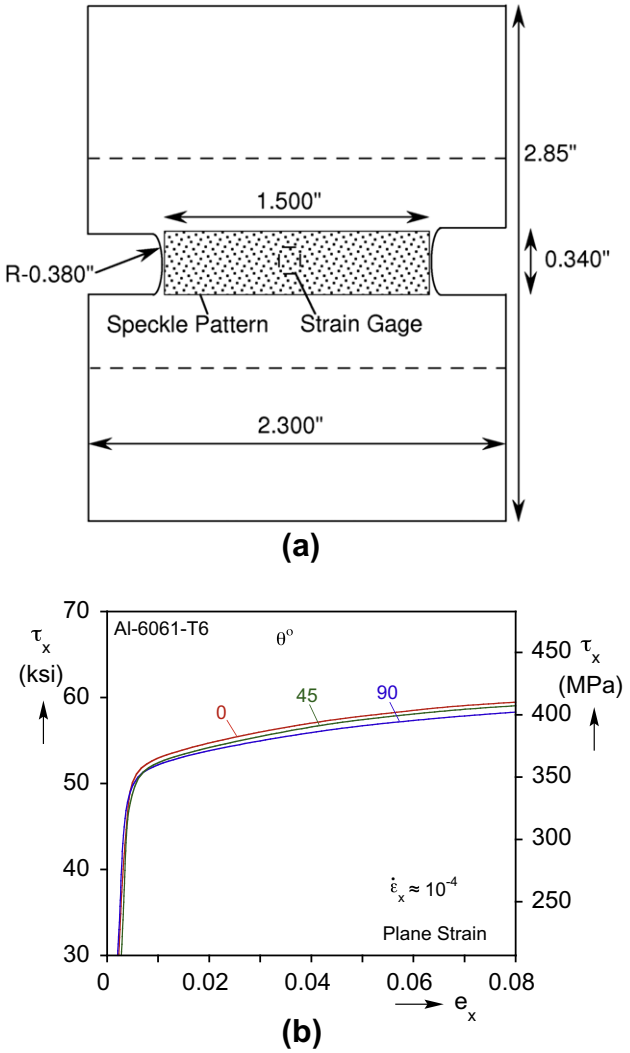

Fig. 10. Plane strain experiments: (a) design of test specimen and (b) recorded axial stress–strain responses in three directions.

$$\phi = |S'_1 - S''_1|^k + |S'_1 - S''_2|^k + |S'_1 - S''_3|^k + |S'_2 - S''_1|^k + |S'_2 - S''_2|^k + |S'_2 - S''_3|^k + |S'_3 - S''_1|^k + |S'_3 - S''_2|^k + |S'_3 - S''_3|^k = 4\sigma_o^k \quad (4)$$

The exponent k is assigned the value of 8 as is typical for FCC alloys (Logan and Hosford, 1980).

3.2. Calibration procedure

We did not have through thickness shear measurements so $\{c'_{44}, c'_{55}, c''_{44}, c''_{55}\}$ were assigned the value 1.0. The rest of the coefficients were determined by minimizing an error function that is described below (similar to the one suggested in Appendix B of Barlat et al. (2005)). Thus for example, for a uniaxial test at an angle θ from the rolling direction the following steps are taken:

The plastic work at several different values of axial stress is determined from the measured responses as follows:

$$W^p = \int_0^{e_{x1}} \tau_x de_x^p \rightarrow \tau_{x\theta}(W^p) \quad (a)$$

The stresses in the material frame (x', y') are given by

$$\boldsymbol{\tau}' = \{\tau_{x'}, \tau_{y'}, \tau_{x'y'}\}^T = \tau_{x\theta}(W^p)\{\cos^2\theta, \sin^2\theta, -\sin\theta\cos\theta\}^T \quad (b)$$

Using the Cauchy stress version of (4),

$$\tau_{e\theta} = [\phi(\boldsymbol{\tau}')/4]^{1/k} \quad (c)$$

and the following error function is established

$$\varepsilon_{\theta a} = \left(\frac{\tau_{e\theta}}{\tau_{x0}(W^p)} - 1\right)^2 \quad (d)$$

where $\tau_{x0}(W^p)$ is the stress at the chosen value of W^p from the basic stress–strain response taken to be the one measured in the rolling direction ($\theta = 0$).

The R_θ values are determined by fitting linearly the measured $e_x^p - e_y^p$, which yields

$$r_{xy} = -\frac{de_y^p}{de_x^p}, \quad \text{and then} \quad R_{\theta ex} = \frac{de_y^p}{de_z^p} = \frac{r_{xy}}{1 - r_{xy}}. \quad (e)$$

Using the flow rule evaluate

$$de'^p_{ij} = d\Lambda \frac{\partial \phi}{\partial \tau'_{ij}} \quad \text{at} \quad \tau'_{ij}. \quad (f)$$

Transform $de'^p_{ij} \rightarrow de^p_{ij}$ and evaluate $\frac{de_y^p}{de_z^p} = R_{\theta\phi}$ and form the error function

$$\varepsilon_{\theta R} = \left(\frac{R_{\theta\phi}}{R_{\theta ex}} - 1\right)^2 \quad (g)$$

This is repeated for each of the seven tensile tests for $W^p = 1000$ psi (6.896 MPa).

For the plane strain tests, W^p is defined again as in (a) with τ_x evaluated as is described in the experimental section and e_x being the strain measured at the center of the specimen. The corresponding τ_y is evaluated using a 3D FE model of the test specimen in which the material was assumed to be isotropic (i.e., Hosford (1)). The calculated value is designated here as $\tau_y = \alpha\tau_x$. (For $\theta = 0$ and 90° $\alpha = 0.4195$ and 0.426 for 45° because the first two specimens were slightly narrower—width 2.00 in) Then

$$\{\tau_{x'}, \tau_{x'}, \tau_{x'y'}\}^T = \{\tau_{x'}, \tau_{x'}, 0\}^T\big|_{W^p} T_1(\theta), \quad (h)$$

where $T_1(\theta)$ is the usual transformation matrix for 2-D stress states. The equivalent stress $\tau_{e\theta}$ based on (τ_x, τ_y) is evaluated from (c) and is compared to τ_{x0} in an error function like the one in (d).

The disk compression strains in Fig. 9 fall on a straight line and thus

$$r_{x'y'} = \frac{de_{y'}^p}{de_{x'}^p} \quad (i)$$

is evaluated at any value of normal stress τ_z. Flow rule (f) is subsequently used to calculate the strain increments in the principal material directions corresponding to stress τ_z. The results are used to form the error function

$$\varepsilon_{dkR} = \left(\frac{r_{x'y'\phi}}{r_{x'y'ex}} - 1\right)^2. \quad (j)$$

The "best" values of the anisotropy coefficients (c'_{ij}, c''_{ij}) are then chosen by minimizing the following weighted sum of these error functions:

$$\varepsilon(c'_{ij}, c''_{ij}) = \sum_m \omega_m \left(\frac{\tau_{e\phi}}{\tau_{x0}} - 1\right)^2_m + \sum_n \omega_n \left(\frac{R_\phi}{R_{ex}} - 1\right)^2_n, \quad (5)$$

where the first series represents the errors from the m flow stresses, the second the errors from the n r-values established, and (ω_m, ω_n) are weight functions that represent the confidence level assigned to each particular experiment (both r and R have been used as defined in above). The minimization was performed using the routine *Nminimize* of Mathematica. The resultant anisotropy constants are listed in Table 1.

Table 1
Anisotropy parameters for Yld04-3D ($k = 8$) determined from the calibration process.

c'_{12}	c'_{13}	c'_{21}	c'_{23}	c'_{31}	c'_{32}	c'_{44}	c'_{55}	c'_{66}
−1.005	−1.078	−1.056	−1.113	1.4418	0.3197	1.0	1.0	0.9796
c''_{12}	c''_{13}	c''_{21}	c''_{23}	c''_{31}	c''_{32}	c''_{44}	c''_{55}	c''_{66}
0.8217	−0.299	0.2708	0.6895	2.1823	2.118	1.0	1.0	0.8222

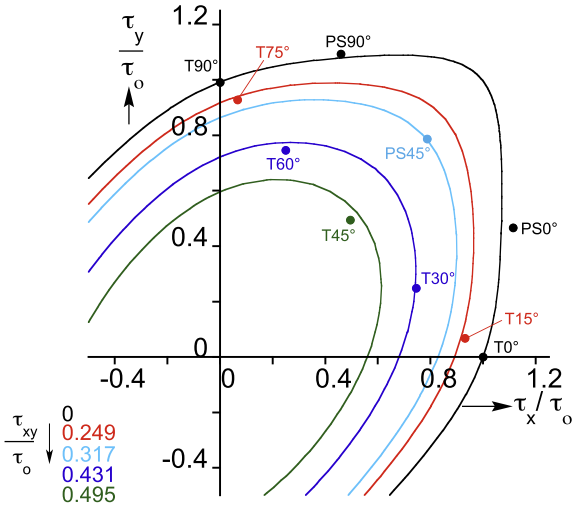

Fig. 11. Calibrated Yld04 3-D yield surfaces for different values of normalized shears and experimental data (solid bullets).

In the way of evaluating the performance of the minimization process the calibrated yield surface and some of the corresponding experimental points are compared in Fig. 11 (T ≡ tension, PS ≡ plane strain). Plotted are the normal stresses (τ_x/τ_o vs. τ_y/τ_o) for different values of normalized shear stress (τ_{xy}/τ_o) where τ_o is the stress in tension in the x-direction at the chosen value of W^p (as in Barlat et al., 2005). The comparison of measurements and the calibrated YS is quite favorable.

4. Finite element simulation of the tensile test

4.1. Modeling

The tensile test described in Section 2a was simulated numerically using a FE model developed in the nonlinear code ABAQUS. Symmetries of the set-up about mid-span, the mid-width and the mid-thickness allowed us to limit attention to 1/8th of the specimen as shown in Fig. 12. The length of the section considered ($2L$) varied from the full length—i.e., from the gripped line to mid-span—to just the length under the extensometer (2.0 in—51 mm). The large radii built into the sides of the specimen were included. The domain was discretized with 8-node linear brick elements with reduced integration and hourglass control (C3D8R). Two, nearly isotropic mesh densities were implemented, a finer one at the center of the specimen about $0.57w_0$ long and a coarser mesh for the rest of the length analyzed. A typical model had 8 or 12 elements through the half thickness in the central section while the coarse domain had 4 elements through the thickness. The

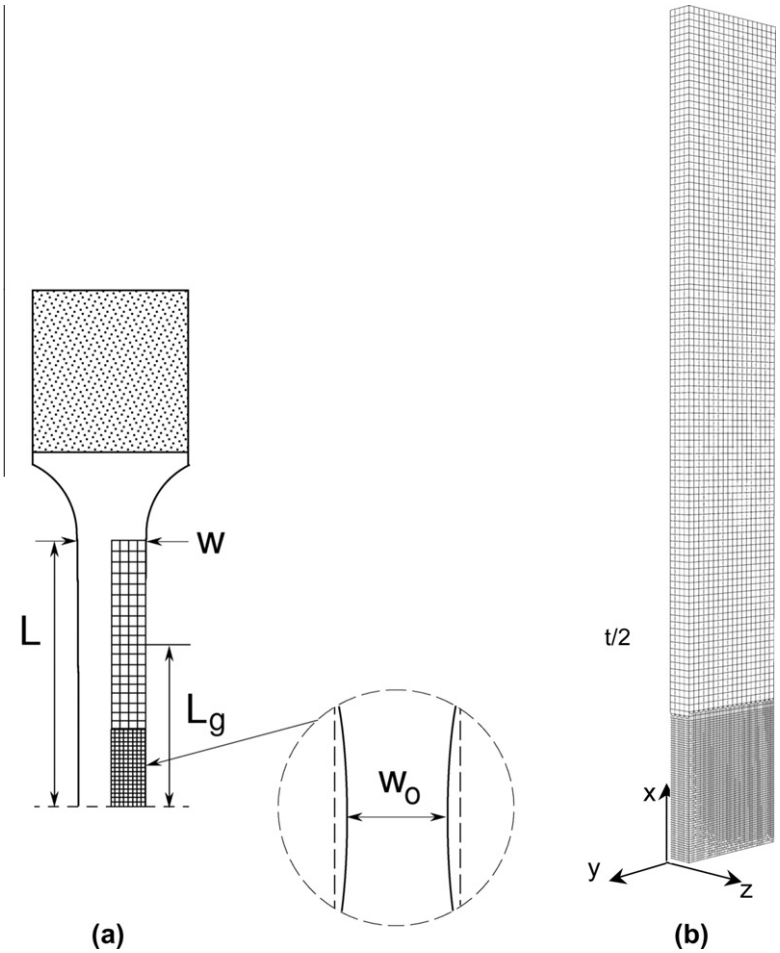

Fig. 12. Finite element model: (a) Domain analyzed and (b) typical mesh (the central section has 8 or 12 elements through the thickness).

elements were essentially isotropic and thus they scaled accordingly in the other two dimensions.

The Yld04-3D constitutive model as calibrated in the previous section was adopted in the calculations using a subroutine developed by Yoon et al. (Yoon et al., 2004, 2006; Yoon, 2009). For comparison, the von Mises (vM) and Hosford with exponent 8 (H8) isotropic yield functions will also be implemented in the simulation of the tensile test.

For each of the yield functions the FE model was used to extract iteratively a true stress-logarithmic strain material response that makes the calculated force-elongation response to match the experimental one shown in Fig. 2. In the simulations the displacement at $x = L$ is prescribed, and the calculated global force and the displacement at $x = L_g$ are monitored. An initial guess of the stress–strain response is generated by adopting the measured true stress-logarithmic strain up to the load maximum, and linearly extrapolating it to higher strains. The calculated force based on this response is compared to the measured one at the same displacement and if there is disagreement between the two the stress is updated and the calculation is repeated. The calculation is completed once the calculated force is within a chosen tolerance to the measured value and the process is repeated for the next displacement increment. Typical displacement increments were of the order of 10^{-4} in (25 μm). The process was found to lead to quick convergence for $\delta/2L_g < 0.09$ whereas at higher displacements, when localization sets in, manual intervention was often necessary.

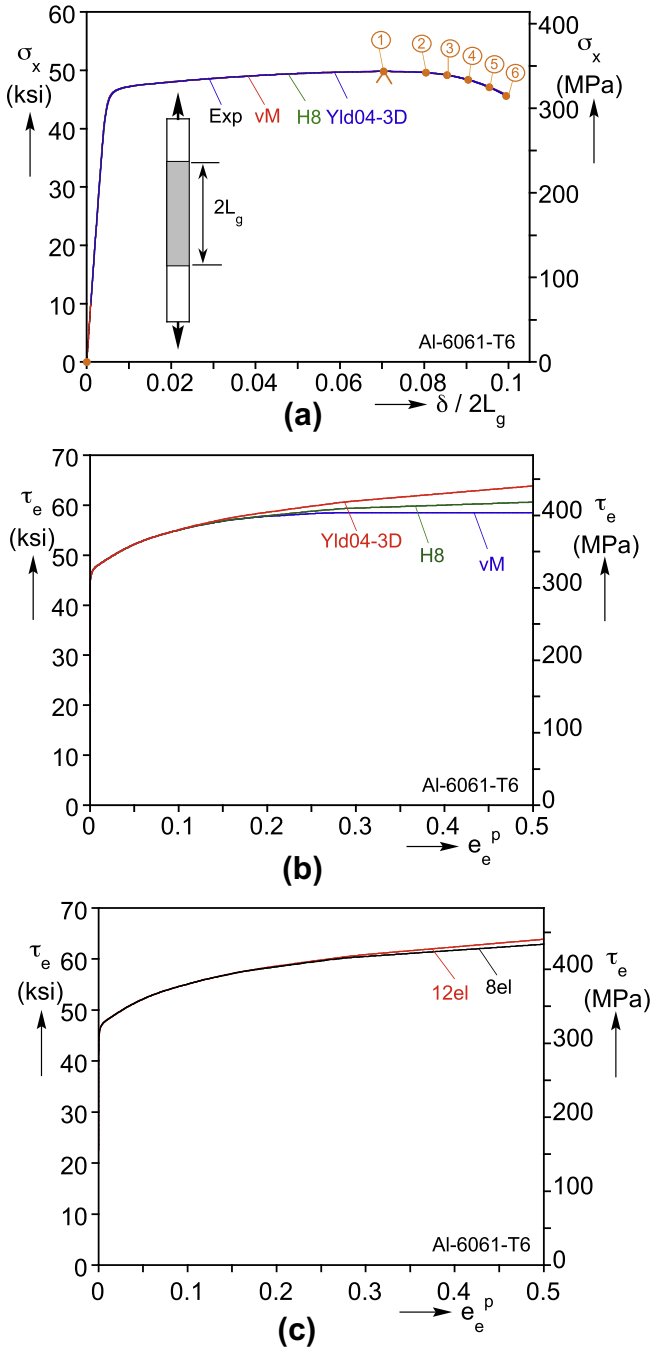

Fig. 13. (a) Comparison of measured force displacement response with the ones calculated using the FE model by iteratively adjusting the basic stress–strain response of the material. Results shown for Yld04-3D, vM, and H8 constitutive models. (b) The extracted equivalent stress-plastic equivalent strain responses. Effect of element mesh on extracted stress-plastic strain response.

Fig. 13a shows a comparison of the measured and the three calculated engineering stress-displacement responses. The agreement between measured and calculated results is very good for Yld03-3D and H8 whereas there is some small deviation for vM for $\delta/2L_g > 0.08$ (this despite the plastic tangent modulus being zero at higher strains). Fig. 13b shows plots of the extracted equivalent stress-plastic equivalent strain using the three models. The three responses exhibit a positive modulus to strains of nearly 50%. They agree for plastic strain less than 10%, but deviate from each other for higher strains. The Yld04-3D model produced the stiffest response, the vM the least stiff one and H8 lies between the two. The results confirm that adoption on a non-quadratic yield function plays a role in the results and that anisotropy, even as modest as the one recorded in the present sheet material, must be included in the extraction calculations.

It is worth mentioning that the extracted responses were found to exhibit sensitivity to the mesh adopted. This sensitivity was primarily observed at higher strains associated with the development of localized deformation bands inside the diffuse in-plane neck. Thus, although the deformations produced by the model with 8 elements through the half thickness compared well with the experimental deformations as measured by the edge detection and in-plane DIC, some difference from the 12-element model was observed in the extracted stress–strain response (see Fig. 13c). This led us to report here the results from the most refined model (see similar observation in Dunand and Mohr, 2010).

The effect of the length of the section modeled was considered. Most calculations were performed with $L = L_g$, but models with lengths of $1.5L_g$ and $2.2L_g$ were also analyzed. No significant effect of the model length was noticed on the extracted material response. In the present set-up where the zone of localization is of the order of $1.5w_0$, a model with an overall length of $4w_0$ suffices. What is more important however, is the need to model the central part of the domain with a fine enough mesh that is capable of capturing the banded localization that develops.

4.2. Performance of the Yld04-3D model

The results of the FE models are now evaluated by directly comparing the predicted neck shapes with the corresponding shapes measured using the edge detection method. In addition, calculated strains will be compared with strains measured via DIC. This comparison is performed for each of the three constitutive models used, using in each model its calibrated stress–strain response (Fig. 13b). Comparisons were performed for each of the six points on the descending part of the force–displacement response identified in Figs. 2 and 13a. Here, for brevity, we will show comparisons for points ①, ④ and ⑥.

Fig. 14a shows comparisons of the measured and calculated profiles of the left and right edges at the limit load (point ① at $\delta/2L_g = 0.07$). At this stage localization has yet to start and thus the edges are nearly circular arcs. The edges from the Yld04-3D model match very well the experimental ones while the ones from the models using vM and H8 exhibit more deformation, a direct results of their isotropic nature. Fig. 14b shows comparisons of the measured and calculated axial strain and transverse strain ratio, e_y/e_x, along the centerline of the test section. The axial strain profile is reproduced very well by all three models. The transverse strain from Yld04 matches the experimental profile very well while the predictions using vM and H8 do not, again due to their isotropic nature.

Fig. 15 shows a similar comparison for point ④ at $\delta/2L_g = 0.09$. Now the diffuse neck is well developed covering a central region approximately $1.5w_0$ long. The calculated edge deflections using Yld04-3D model are seen in Fig. 15a to match well the measured edge profiles while the vM and H8 models produce much deeper necks. The axial strains along the centerline of the specimen are again predicted well by all three models apparently because this deformation is not affected significantly by anisotropy. By contrast, the transverse strain ratio is again over-predicted by vM and H8 and is captured well by Yld04-3D.

The final comparison in Fig. 16 is for point ⑥ on the force–displacement response corresponding to the end of the test (at $\delta/2L_g = 0.10$). The significant deepening of the neck is captured

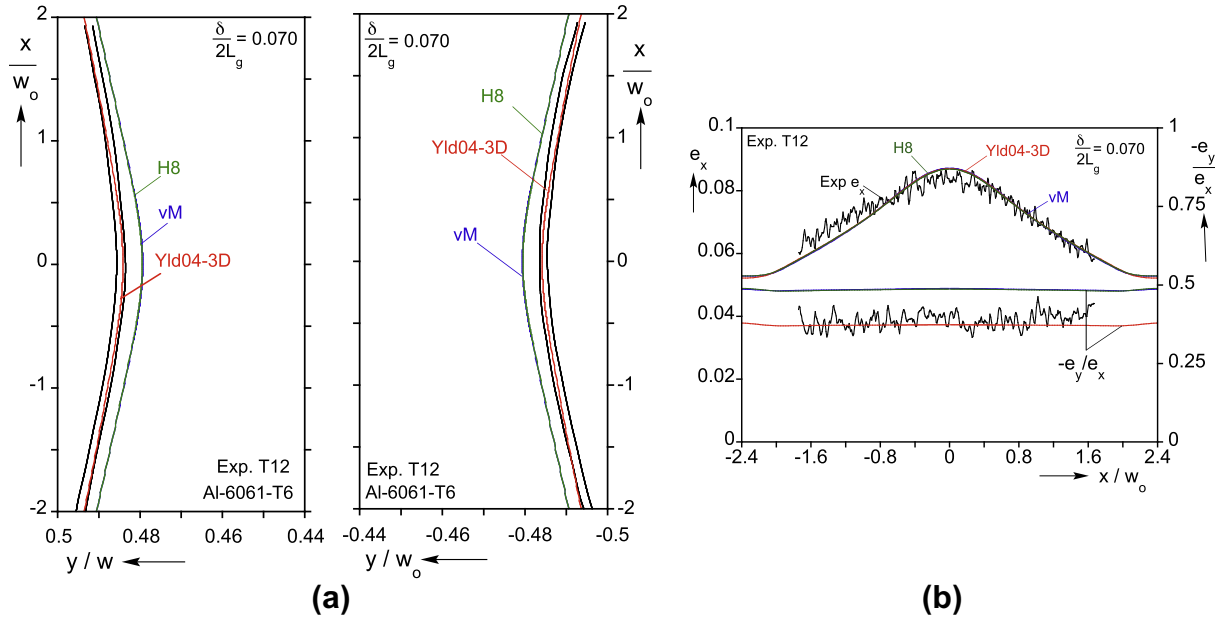

Fig. 14. Comparison of measured and calculated neck region deformations for $\delta/2L_g = 0.07$: (a) Left and right edges and (b) axial and transverse strains along centerline of specimen.

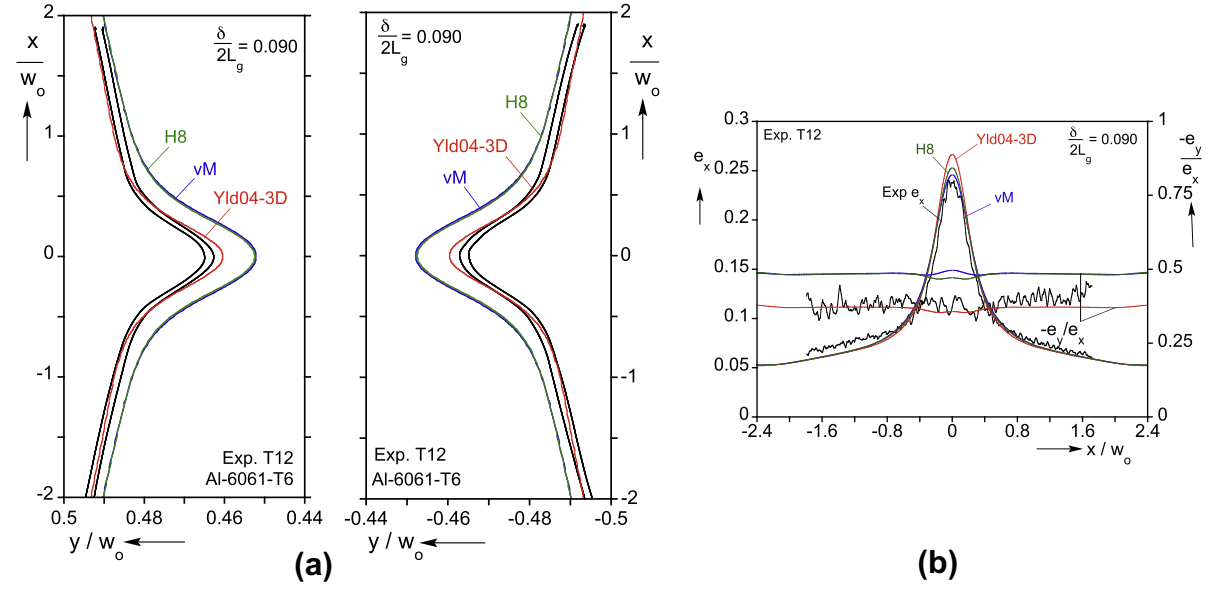

Fig. 15. Comparison of measured and calculated neck region deformations for $\delta/2L_g = 0.09$: (a) Left and right edges and (b) axial and transverse strains along centerline of specimen.

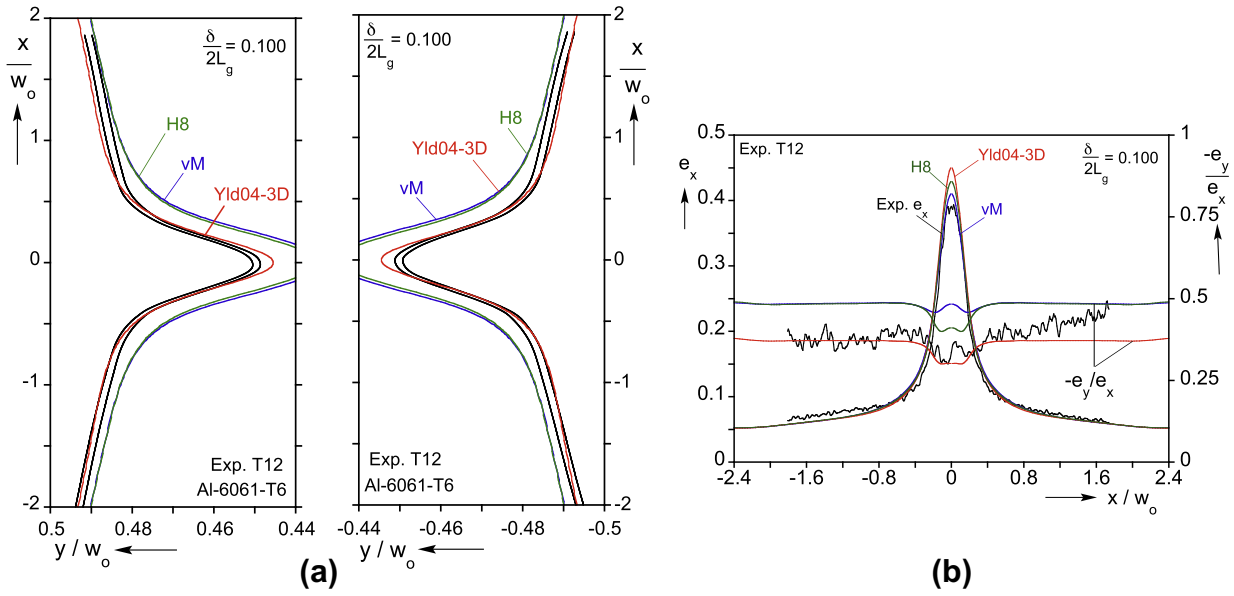

Fig. 16. Comparison of measured and calculated neck region deformations for $\delta/2L_g = 0.10$: (a) Left and right edges and (b) axial and transverse strains along centerline of specimen.

well by Yld04-3D and is significantly over-predicted by the other two models. The axial strain predictions yielded by the three models are again very similar and agree with the measurements. A small disagreement is observed at the very center of the specimen ($x = 0$). It must be pointed out however that the resolution of our DIC was not capable of capturing the relatively abrupt changes in strain that take place in this narrow zone. The transverse strain ratio profiles are similar to those of the previous two cases, with the results from Yld04-3D agreeing with the experimental ones and those from the two isotropic models being at variance. One detail in the strain ratios is the development of a small depression at the center of the specimen that can be seen in the experimental results despite the noise in the profile. This is captured well by Yld04-3D and H8 but has an opposite sign for vM.

Finally, it is of interest to reiterate that the very good agreement between the measured and calculated deformation in the zone of localization reported in Figs. 14–16 was achieved with a monotonic material response. Support for this notion also comes from a recent parallel study on the same Al alloy sheet that involves detailed microscopy analysis of necking and failure by Ghahremaninezhad and Ravi-Chandar (in press); they reported that no damage was observed for strains of nearly 100%. This suggests that great caution should be exercised before embarking in ad hoc introduction of softening to constitutive models in order to capture various localization events, as is the recent trend.

5. Summary and conclusions

We have presented a systematic methodology that uses a combination of experiment and analysis to extract the material response of sheet metal at large strains. The method involves a tensile test on a custom test specimen during which the force–displacement response is recorded. The response exhibits a load maximum at a strain of a few percent followed initially by diffuse necking and at a later stage by localization along inclined bands. During the test the deformation in the necked zone was monitored using an edge detection technique and 2-D DIC. The test is simulated numerically using a 3D FE model and the material response is iteratively extrapolated until the calculated and measured force–displacement responses match.

For the Al-6061-T6 sheet metal of interest, the extracted response is influenced by inherent anisotropies introduced during the rolling process. The anisotropy was characterized by conducting a set of uniaxial and biaxial tests on the same sheet metal. The results were used to calibrate the 18-parameter non-quadratic Yld04-3D yield function. Yld04-3D was implemented in the FE model used to simulate the tensile test while simultaneously extracting the material response. Stress–strain responses were also generated in similar FE calculations for the von Mises and Hosford yield functions. The results of the simulations were subsequently evaluated by comparing the calculated deformations with the corresponding measured strains and evolution of the shape of the neck. The following observations and conclusions can be drawn from the results.

(a) The three extracted material responses exhibit a positive modulus to strains of nearly 50%. They do not resemble any of the standard stress–strain fits (similar observation made in Dunand and Mohr (2010) for TRIP steel). In addition, in a parallel micromechanical study of localization and failure in the same material, Ghahremaninezhad and Ravi-Chandar (in press) observed no damage in the necked zone up to strain of nearly 100%. Although these results and observations are material dependent, they should cause pause to the recent trend of ad hoc introduction of softening to constitutive models in order to capture various localization events.

(b) The Yld04-3D model produced the stiffest response, the vM the least stiff one and H8 one that lies between the two. The results confirm that adoption on a non-quadratic yield function plays a role in the calculations and that anisotropy, even as modest as the one recorded in the present sheet material, must be included in the model used to extract the response.

(c) The process used to calibrate the 18-parameter Yld04-3D anisotropic yield function is rather cumbersome and the calculated constants are not necessarily unique. Because of lack of information we assumed that the material is isotropic to through thickness shear. The role of this assumption should be further scrutinized perhaps by augmenting the experimental results with crystal plasticity calculations as

suggested in Barlat et al. (2005). A biaxial test such as the bulge test, with detailed measurement of the deformation at the apex, would help the calibration. We also assumed that the anisotropy does not evolve during deformation, an assumption that is reasonable for the Al-6061-T6 sheet metal analyzed.

Acknowledgements

The authors acknowledge with thanks financial support from the Office of Naval Research through the MURI project N00014-06-1-0505-A00001. Special thanks go to Dr. Jeong-Whan Yoon of Swinburne University of Technology, for providing his subroutine for the Yld2004-3D model used in this work, and to Y. Korkolis for the benefit of several helpful discussions on this work.

References

Aretz, H., Aegerter, J., Engler, O., 2010. Analysis of earing in deep drawn cups. In: Proc. NUMIFORM 2010, Pohang University, Korea, June 13–17, 2010.

Banabic, D., Aretz, H., Cosma, D.S., Paraianu, L., 2005. An improved analytical description of orthotropy in metallic sheets. Int. J. Plast. 21, 493–512.

Barlat, F., Lian, K., 1989. Plastic behavior and stretchability of sheet metals. Part I: A yield function for orthotropic sheets under plane stress conditions. Int. J. Plast. 5, 51–66.

Barlat, F., Brem, J.C., Yoon, J.W., Chung, K., Dick, R.E., Lege, D.J., Pourboghrat, F., Choi, S.-H., Chu, E., 2003. Plane stress yield function for aluminum alloy sheets-Part 1: theory. Int. J. Plast. 19, 1297–1319.

Barlat, F., Aretz, H., Yoon, J.W., Karabin, M.E., Brem, J.C., Dick, R.E., 2005. Linear transformation-based anisotropic yield functions. Int. J. Plast. 21, 1009–1039.

Bridgman, P.W., 1944. The stress distribution at the neck of a tension specimen. Trans. Am. Soc. Met. 32, 553–574.

Cai, W.W., Carsley, J.E., Hayden, D.B., Hector, Jr., L.G., Stoughton, T.B., 2007. Estimation of metal hardening models at large strains. In: Proc. Int. Manuf. & Eng. Conf., MSEC2007-31137, Oct. 2007, Atlanta, Georgia.

Chen, W.H., 1971. Necking of a bar. Int. J. Solids Struct. 7, 685–717.

Dunand, M., Mohr, D., 2010. Hybrid experimental-numerical analysis of basic ductile fracture experiments for sheet metals. Int. J. Solids Struct. 47, 1130–1143.

Ghahremaninezhad, A., Ravi-Chandar, K., in press. Ductile failure in polycrystalline aluminum alloy Al 6061-T6. Int J. Fracture. doi:10.1007/s10704-012-9689-z.

Giagmouris, T., Kyriakides, S., Korkolis, Y.P., Lee, L.-H., 2010. On the localization and failure in aluminum shells due to crushing induced bending and tension. Int. J. Solids Struct. 47, 2680–2692.

Hill, R., 1979. Theoretical plasticity of textured aggregates. Math. Proc. Cambridge Philosophical Society 85, 179–191.

Hill, R., 1990. Constitutive modeling of orthotropic plasticity in sheet metals. J. Mech. Phys. Solids 38, 405–417.

Hosford, W.F., 1972. A generalized isotropic yield criterion. ASME J. Appl. Mech. 39, 607–609.

Hosford, W.F., 1979. On yield loci of anisotropic cubic metals. In: Proceedings of the 7th North American Metalworking Research Conference, Society of Manufacturing Engineers, Dearborn, MI, pp. 191–196.

Karafillis, A.P., Boyce, M.C., 1993. A general anisotropic yield criterion using bounds and a transformation weighting tensor. J. Mech. Phys. Solids 41, 1859–1886.

Korkolis, Y.P., Kyriakides, S., 2008a. Inflation and burst of anisotropic aluminum tubes for hydroforming applications. Int. J. Plast. 24, 509–543.

Korkolis, Y.P., Kyriakides, S., 2008b. Inflation and burst of anisotropic aluminum tubes Part II: An advanced yield function including deformation-induced anisotropy. Int. J. Plast. 24, 1625–1637.

Korkolis, Y.P., Kyriakides, S., 2009. Path-dependent failure of inflated aluminum tubes. Int. J. Plast. 25, 2059–2080.

Korkolis, Y.P., Kyriakides, S., Giagmouris, T., Lee, L.-H., 2010. Constitutive modeling and rupture predictions of Al-6061-T6 tubes under biaxial loading paths. ASME J. Appl. Mech. 77 (5), 23, 064501, 1–5.

Korkolis, Y.P., Kyriakides, S., 2011. Hydroforming of anisotropic aluminum tubes. Part II: Analysis. Int. J. Mech. Sci. 53, 83–90.

Logan, R.W., Hosford, W.F., 1980. Upper-bound anisotropic yield locus calculations assuming <111>-pencil glide. Int. J. Mech. Sci. 22, 419–430.

Norris Jr., D.M., Moran, B., Scudder, J.K., Quinones, D.F., 1978. A computer simulation of the tension test. J. Mech. Phys. Solids 26, 1–19.

Scheider, I., Brocks, W., Corneck, A., 2004. Procedure for the determination of true stress–strain curves from tensile tests with rectangular cross-section specimens. ASME J. Eng. Mater. Technol. 126, 70–76.

Swift, H.W., 1952. Plastic instability under plane stress. J. Mech. Phys. Solids 1, 1–18.

Tvergaard, V., 1993. Necking in tensile bars with rectangular cross-section. Comp. Meth. Appl. Mech. Eng. 103, 273–290.

Voce, E., 1948. The relationship between stress and strain for homogeneous deformation. J. Inst. Met. 74, 537–562.

Wagoner, R.H., 1981. Comparison of plane-strain and tensile work hardening in two sheet steel alloys. Met. Trans. A 12, 877–882.

Yoon, J.W., Barlat, F., Dick, R.E., Chung, K., Kang, T.-J., 2004. Plane stress yield function for aluminum alloy sheets—part II: FE formulation and its implementation. Int. J. Plast. 20, 495–522.

Yoon, J.W., Barlat, F., Dick, R.E., Karabin, M.E., 2006. Prediction of six or eight ears in a drawn cup based on a new anisotropic yield function. Int. J. Plast. 22, 174–193.

Yoon, J.W., 2009, 2011. Personal communication.

Zhang, Z.L., Hauge, M., Ødegård, J., Thaulow, C., 1999. Determining material true stress–strain curve from tensile specimens with rectangular cross section. Int. J. Solids Struct. 36, 3497–3516.